Suppression of nematicity by tensile strain in multilayer FeSe/SrTiO$_3$ films

Rui Lou [1,2,3,*], Oleksandr Suvorov,[1,4] Hans-Joachim Grafe [1], Andrii Kuibarov,[1] Maxim Krivenkov [2], Oliver Rader,[2]
Bernd Büchner,[1,5] Sergey Borisenko,[1,†] and Alexander Fedorov[1,2,3,‡]

[1]*Leibniz Institute for Solid State and Materials Research, IFW Dresden, 01069 Dresden, Germany*
[2]*Helmholtz-Zentrum Berlin für Materialien und Energie, Albert-Einstein-Straße 15, 12489 Berlin, Germany*
[3]*Joint Laboratory "Functional Quantum Materials" at BESSY II, 12489 Berlin, Germany*
[4]*G. V. Kurdyumov Institute for Metal Physics of the N.A.S. of Ukraine, 03142 Kyiv, Ukraine*
[5]*Institute for Solid State and Materials Physics, TU Dresden, 01062 Dresden, Germany*

The nematicity in multilayer FeSe/SrTiO$_3$ films has been previously suggested to be enhanced with decreasing film thickness. Motivated by this, there have been many discussions about the competing relation between nematicity and superconductivity. However, the criterion for determining the nematicity strength in FeSe remains highly debated. The understanding of nematicity as well as its relation to superconductivity in FeSe films is therefore still controversial. Here, we fabricate multilayer FeSe/SrTiO$_3$ films using molecular beam epitaxy and study the nematic properties by combining angle-resolved photoemission spectroscopy, ^{77}Se nuclear magnetic resonance, and scanning tunneling microscopy experiments. We unambiguously demonstrate that, near the interface, the nematic order is suppressed by the SrTiO$_3$-induced tensile strain; in the bulk region further away from the interface, the strength of nematicity recovers to the bulk value. Our results not only solve the recent controversy about the nematicity in multilayer FeSe films, but also offer valuable insights into the relationship between nematicity and superconductivity.

I. INTRODUCTION

Electronic nematicity, which breaks rotational symmetry but preserves translational symmetry of a lattice [1], has been widely observed in cuprates [2–5] and iron-based superconductors [6–12]. In iron-based superconductors, nematicity is usually accompanied by a tetragonal-to-orthorhombic structural transition [13]; in addition, collinear antiferromagnetism sets in at or just below the nematic transition in iron pnictides [14,15]. The complicated coupling between lattice, spin, and orbital degrees of freedom [10,16,17] renders the origin of nematicity controversial [18–21]. FeSe is an attractive system to explore the effect of nematicity disentangled from that of magnetic order, as it exhibits nematicity below $T_{nem} \sim$ 90 K without long-range magnetic order at any temperature [22–27]. FeSe also provides a versatile platform for studying the interplay of nematicity and superconductivity since the superconductivity therein is highly tunable [28–36].

The relationship between nematicity and superconductivity is under hot debate in FeSe crystals. Their competition is proposed in an electron irradiation experiment, where the disorder enhances T_c while it lowers T_{nem} [37], as hydrostatic

pressure [38] and uniaxial strain do [39,40]. Their cooperative effect is suggested by the sizable enhancement of T_c with an enlarged orthorhombic distortion below T_c upon increasing sulfur doping in FeSe [41]. Contrary to a direct correlation, thermal-expansion measurements find a lack of coupling between nematicity and superconductivity [42].

Thus the origin of nematicity in FeSe remains highly interesting, but its effect on the electronic structure is controversial. In FeSe crystals, due to the complicated band structure and multiorbital character around the Brillouin zone (BZ) corner, the energy scale of the zone-corner d_{xz}/d_{yz} splitting has been hotly debated. It was reported to be either $\sim$50 meV [25,26,43–45] or degenerate [46,47], questioning whether the bands at the BZ corner are appropriate for understanding the nematicity. Instead, the relatively simple band structure around the BZ center provides a remarkable platform, by which the nematic energy scale of $\sim$15–20 meV agrees with the T_{nem} scale [26,46–48]. In multilayer FeSe/SrTiO$_3$ films, it has been previously suggested that the strength of nematicity in thinner FeSe films is stronger than that in FeSe crystals, and it further enhances with decreasing thickness [34,49–52]. However, in these studies, the nematicity strength was determined by the band splitting around the BZ corner, and the validity of this criterion has been questioned in FeSe crystals [53]. Therefore, whether the nematicity is enhanced in thinner FeSe films is still an open question.

Herein we present combined angle-resolved photoemission spectroscopy (ARPES), ^{77}Se nuclear magnetic resonance (NMR), and scanning tunneling microscopy (STM) studies on multilayer FeSe/SrTiO$_3$ films. NMR measurements show the coexistence of single-domain and twinned-domain structures in 210-monolayer (ML) film; as 15-ML film forms a

*lourui09@gmail.com
†s.borisenko@ifw-dresden.de
‡a.fedorov@ifw-dresden.de

single domain revealed by STM, we suggest that the former structure is near the interface and the latter one is from the bulk region further away from the interface under noticeable and negligible tensile strains, respectively. Consistently, in 15-ML film, the single circular hole Fermi surface (FS) and the temperature-independent d_{xz}/d_{yz} splitting around $\bar{\Gamma}$ indicate the absence of nematicity; in 115-ML film, the splitting of the outer hole band and the temperature evolutions of d_{xz} and d_{yz} orbitals at $\bar{\Gamma}$ validate the emergence of bulklike nematicity.

II. EXPERIMENTAL METHODS AND DETAILS

A. Film growth

The multilayer FeSe films were fabricated on either Nb:SrTiO$_3$(001) (for ARPES and STM) or SrTiO$_3$(001) (for NMR) substrates (both denoted as SrTiO$_3$ substrate hereafter) with atomically flat TiO$_2$ terminations, which were formed by treating the substrates with Se molecular beam etching method prior to film growth [33]. A standard Knudsen cell and a thermal cracker effusion cell were used to evaporate Fe and Se, respectively. The substrates were kept at $530\,^\circ$C during the evaporation. The as-grown films were subsequently annealed at $560\,^\circ$C for 3 hours. After the growth, the samples were transferred to the ARPES end station and a separate STM chamber via a vacuum suitcase with a base pressure of 1×10^{-9} Torr.

B. ARPES

ARPES measurements were performed using the 1^2-ARPES end station of the UE-112-PGM2 beamline at the Helmholtz Zentrum Berlin BESSY-II light source. The energy and angular resolutions were set to better than 5 meV and 0.1°, respectively. During the experiments, the sample temperature was kept at 15 K if not specified otherwise, and the vacuum conditions were maintained better than 6×10^{-11} Torr.

C. STM

STM data were acquired using an Omicron LT-STM system at the base temperature of ~4.5 K. An electrochemically etched polycrystalline tungsten tip was used for the measurements; further *in situ* tip preparation is described elsewhere [54].

D. NMR

NMR measurements were done in a 16-T Oxford magnet with a field homogeneity of 10 ppm over 1 cm^3. The 210-ML FeSe sample had a dimension of about 0.8×1 cm^2, and was mounted on a surface coil with a diameter of about 0.9 cm, similar to the design in Ref. [55]. The field was set to 14 T, and calibrated to be 13.977 T with ^{63}Cu NMR of a piece of Cu wire in the center of the coil (gyromagnetic ratio of ^{63}Cu metal: $^{63}\gamma = 11.312$ MHz/T).

The same magnet was used for the single crystal measurements of FeSe$_{0.95}$S$_{0.05}$ [56], and calibrated to be exactly 11 T by ^{63}Cu NMR of the coil. This gives an absolute value of the Knight shift of about $K_{ab} = 0.16\%$ at low temperatures (average of the split spectrum, $^{77}\gamma = 8.13$ MHz/T, $\boldsymbol{a} \parallel$ [100], $\boldsymbol{b} \parallel$ [010], $\boldsymbol{c} \parallel$ [001]). Note that the Knight shifts at low tem-
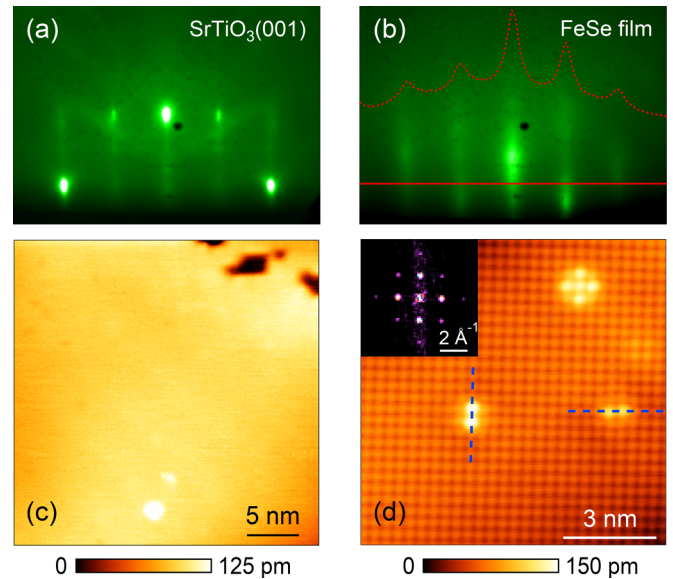

FIG. 1. [(a),(b)] RHEED images of SrTiO$_3$ substrate and 15-ML film with incident beam along the [110] directions, respectively. The RHEED intensity curve (red dashed curve) is taken along the red solid line. The single set of diffraction peaks reflect the high quality of FeSe film. (c) STM topographic image of 15-ML film (30×30 nm^2, $V_s = 50$ mV, $I = 50$ pA). (d) Atomically resolved STM topography of 15-ML film (10×10 nm^2, $V_s = 50$ mV, $I = 100$ pA). Blue dashed lines indicate the orientations of Fe vacancies. Inset: Fourier transform (FT) of the defect-free regions in (d).

peratures in other studies of FeSe crystals range from $K_{ab} = 0.31\%$ ($K_c = 0.293\%$) [24], $K_{ab} = 0.26\%$ ($K_c = 0.24\%$) [27], $K_{ab} = 0.296\%$ ($K_c = 0.28\%$) [57], to $K_c = 0.13\%$ [58]. The differences may stem from different calibration procedures. However, the temperature dependencies of the Knight shifts in the different studies are the same, and are much weaker than in the FeSe film studied here (see detailed discussion in Appendix D).

We estimated the total number of Se nuclei in a 210-ML FeSe film of 0.8 cm^2 to be about 3×10^{17}. The natural abundance of ^{77}Se, the only NMR active isotope, is only 7.5%, so that there are about 2×10^{16} NMR active Se nuclei in the FeSe film. An FeSe single crystal of typical dimension $1 \times 0.5 \times 0.1$ mm^3 has about five times more ^{77}Se nuclei, and therefore a much better NMR signal-to-noise ratio.

III. SURFACE AND STRUCTURAL CHARACTERIZATION OF 15-ML FeSe FILM

The surface and structural characterization of 15-ML film are presented in Fig. 1. Figures 1(a) and 1(b) show the reflection high-energy electron diffraction (RHEED) patterns of SrTiO$_3$ substrate and 15-ML film at room temperature, respectively. A typical STM topographic image of 15-ML film at ~4.5 K is displayed in Fig. 1(c), where the surface consists of a single crystallographic domain. The single-domain feature is observed in a number of scan areas over the sample surface, unlike the presence of twinned domains with twin boundaries previously reported in thicker FeSe films [59] and FeSe crystals [60]. The atomic-resolution STM image and its Fourier
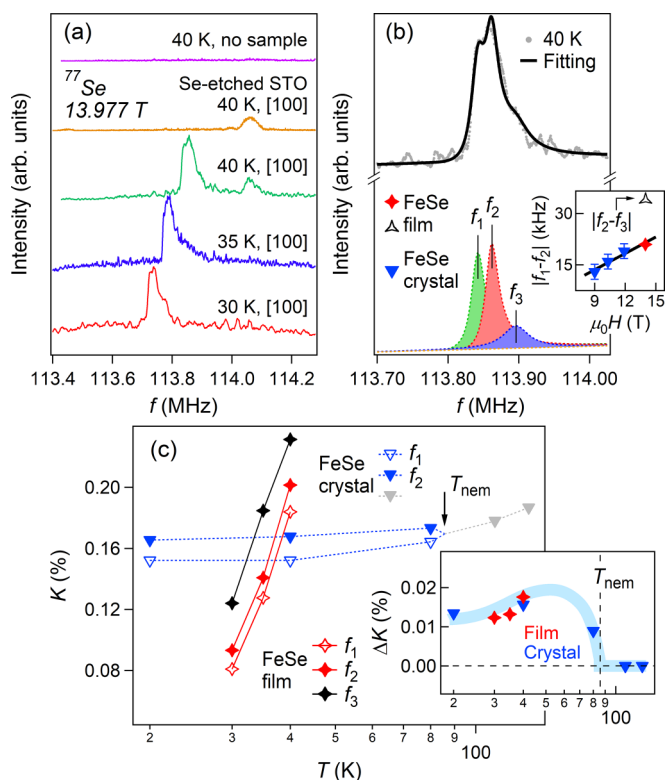
FIG. 2. (a) ^{77}Se NMR spectra of 210-ML film and Se-etched SrTiO$_3$ substrate. (b) Multipeak fitting of the green curve in (a) by three Lorentzian peaks (dashed curves) with a linear background (dashed line). Inset: Frequency splitting between f_1 and f_2 at 40 K as a function of field. Blue triangles represent the values of undoped FeSe crystals, adopted from Refs. [24,57,63]. Black triangle indicates the splitting between f_2 and f_3 of FeSe film at 40 K. The thick line is a guide to the eye. (c) Temperature dependent ^{77}Se NMR Knight shift of 210-ML film and FeSe$_{0.95}$S$_{0.05}$ crystal ($H \parallel$ [100]). Inset: Temperature dependence of Knight shift splittings between f_1 and f_2 lines in the film and crystal. The translucent blue curve is a guide to the eye.

transform in Fig. 1(d) reveal a squarelike lattice of the topmost Se atoms. As in previous studies [59–62], the Fe (dumbbell-like) and Se (crosslike) vacancies are observed. Recently, the appearance of stripe patterns pinned around the Fe vacancies has been proposed as a signature of the nematicity-related orthorhombicity in FeSe films [59]; the interaction between the stripes and Fe vacancies has been suggested to induce strong distortions of the latter, such that the directions of the dumbbell shapes show obvious deviation from the Se-Se lattice [59]. However, in 15-ML film [Fig. 1(d)], we do not observe such stripe patterns near the dumbbell-like impurities; as indicated by the blue dashed lines, the Fe vacancies are well aligned along the directions of the Se-Se lattice, showing no evident distortions. These facts indicate the absence of orthorhombicity in 15-ML film.

IV. ^{77}Se NMR MEASUREMENTS OF 210-ML FeSe FILM

To further clarify the domain structure of our films, we conduct NMR measurements on 210-ML film. Figure 2(a)

shows the frequency-swept NMR spectra of the ^{77}Se nuclei for a magnetic field of 13.977 T. At $T = 40$ K, a prominent line ($\sim$113.85 MHz) and a much weaker signal ($\sim$114.06 MHz) are revealed on the sample for $H \parallel$ [100], which are attributed to the FeSe film and Se-etched SrTiO$_3$ substrate, respectively (see Fig. 5 and Appendix A for more discussion on the assignment). Upon cooling, the spectra of FeSe film shift to lower frequencies with a decrease of the linewidth. But it is difficult to observe a signal below 30 K and above 40 K; this limited temperature range for a decent NMR signal is due to the longer spin-lattice relaxation time and smaller nuclear spin polarization at lower and higher temperatures, respectively (see more discussion in Appendix B). By a closer look, we notice that several components are contained in the spectra of FeSe film, including a double-peak splitting and a shoulder. The quantitative fit of the spectra in Figs. 2(b) and 6 (see details of the fitting procedure in Appendix C) validate that each line consists of three Lorentzian peaks with central frequencies f_1, f_2, and f_3, unlike only two split peaks in the nematic phase of FeSe crystals (evidence for the twinned orthorhombic domains) [24,57,63]. In the inset of Fig. 2(b), we plot the nematicity-related frequency splitting of FeSe crystals at 40 K under different fields (blue triangle, adopted from Refs. [24,57,63]) together with $|f_1 - f_2|$ (red star) and $|f_2 - f_3|$ (black triangle) of FeSe film at 40 K. One obtains that $|f_1 - f_2|$ of FeSe film follows the linear field dependence of frequency splitting of FeSe crystals, while $|f_2 - f_3|$ noticeably deviates from the trend. This implies that the f_1-f_2 splitting in FeSe film may arise from the twinned nematic domains like that in FeSe crystals. The f_3 line could then be attributed to a single-domain structure.

In Fig. 2(c), we present the temperature evolution of ^{77}Se Knight shift of FeSe film and FeSe$_{0.95}$S$_{0.05}$ crystal [56]. The Knight shift is determined from $K = (f_{res} - \gamma B)/\gamma B$, where f_{res} is the peak frequency of NMR spectrum, $\gamma = 8.13$ MHz/T is the nuclear gyromagnetic ratio for ^{77}Se, and B is the external field. Although the Knight shifts in the film show much stronger temperature dependence than that in the crystal (see more discussion in Appendix D), their Knight shift splittings between f_1 and f_2 lines at low temperatures, $\Delta K = K_2 - K_1 \propto |f_1 - f_2|$, are comparable and exhibit similar temperature behavior [inset of Fig. 2(c)]. This similarity between film and crystal further demonstrates that the f_1-f_2 splitting in FeSe film is the signature of twinned domains associated with nematicity. Therefore, the single-domain (f_3) and twinned-domain (f_1-f_2) structures are revealed to coexist in 210-ML film. The former one is reminiscent of the single-domained 15-ML film (see Appendix E for the challenge of detecting its single-domain structure by NMR), where the SrTiO$_3$-induced tensile strain has been found to be sizable and isotropic [34]. We thus suggest that the single domain is most likely confined to a region near the interface with noticeable strain effect; accordingly, the twinned domains come from the bulk region further away from the interface with negligible strain effect. This assignment is further validated by the intensity contrast between f_3 and f_2 peaks [Figs. 2(b) and 6], whose intensity ratio (Table I) can be regarded as the volume proportion between these two regions.

TABLE I. Fitting parameters of the Lorentzian and Gaussian profiles.

Lorentzian fit	f_1 (MHz)	f_2 (MHz)	f_3 (MHz)	Intensity $f_3/(f_2 + f_3)$	Intensity f_3/f_2	BG
40 K	113.842	113.862	113.896	0.174	0.211	Linear
35 K	113.778	113.793	113.843	0.180	0.220	Linear
30 K	113.725	113.739	113.774	0.186	0.229	Linear
Gaussian fit	f_1 (MHz)	f_2 (MHz)	f_3 (MHz)	Intensity $f_3/(f_2 + f_3)$	Intensity f_3/f_2	BG
40 K	113.842	113.862	113.896	0.221	0.284	Linear
35 K	113.778	113.793	113.843	0.229	0.297	Linear
30 K	113.725	113.739	113.774	0.240	0.316	Linear

V. ARPES MEASUREMENTS OF 15- AND 115-ML FeSe FILMS

Given that the domain structure in FeSe film evolves with the thickness, we study the electronic structures of 15- and 115-ML films by ARPES measurements. It has been suggested that vacuum-ultraviolet ARPES detects the signals of escaped photoelectrons mainly from the top two FeSe layers [34]. This ensures that the differences between 15- and 115-ML films observed below are essentially of tensile-strain-effect origin. The FS mapping [Fig. 3(a)] and band dispersions along the $\bar{\Gamma}$-$\bar{M}$ direction [Fig. 3(b)] of 15-ML film are analogous to previous results of multilayer FeSe films [34,64]. Due to the complicated band structure around $\bar{M}$ in FeSe, the orbital assignment of multiple 3d bands and the energy scale of d_{xz}/d_{yz} splitting at $\bar{M}$ are controversial [25,26,43–48,53,65,66]. Hereafter, we focus on the relatively simple band structure around $\bar{\Gamma}$. Although the 15-ML film and detwinned FeSe crystal share the similarity of single-domain structure, there is no preferred orientation for the film under SrTiO₃-induced tensile strain, distinct from the uniaxial strain mechanically added to the crystal [45,47,67,68]. Thus, the former has tetragonal structure illustrated by STM while the latter shows orthorhombicity (see Appendix F for a discussion on the distinct NMR spectra caused by this structural difference). As a result, the ellipselike hole pocket in Fig. 3(a) strongly contrasts with that in detwinned FeSe crystal below T_{nem} [45,47,67,68], reflected in their completely different photon polarization dependence (see Fig. 8 and Appendix G for more discussion).

We further measure the band structure along $\bar{\Gamma}$-$\bar{M}$ and $\bar{\Gamma}$-$\bar{X}$ directions in $k_z = 0$ [Figs. 3(c)–3(e)] and π [Figs. 3(f)–3(h)] planes of 15-ML film. As evidenced by the single set of peaks in momentum distribution curves (MDCs) along the $\bar{\Gamma}$-$\bar{M}$ directions [blue curves in Figs. 3(e) and 3(h)], no splitting is observed on the α band when crossing E_F. The hole pocket is further revealed to be circular in shape by comparing the k_F's along $\bar{\Gamma}$-$\bar{M}$ and $\bar{\Gamma}$-$\bar{X}$ directions. In light of this, the ellipselike FSs in Figs. 3(a) and 8 are actually some segments of the circular pocket. In contrast, the FS of twinned FeSe crystals below T_{nem} consists of two crossed elliptical pockets at $\bar{\Gamma}$ arising from the split α band [26,48,69]. The splitting is due to the dispersions of d_{xz}/d_{yz} bands being different for the two twinned domains, and has therefore been suggested as direct evidence for nematicity [26,46,48,69,70]. In a previous study of FeSe$_{1-x}$S$_x$ crystals [69], with the reduction of T_{nem} by the increasing sulfur doping [71], the degree of FS anisotropy at $\bar{\Gamma}$
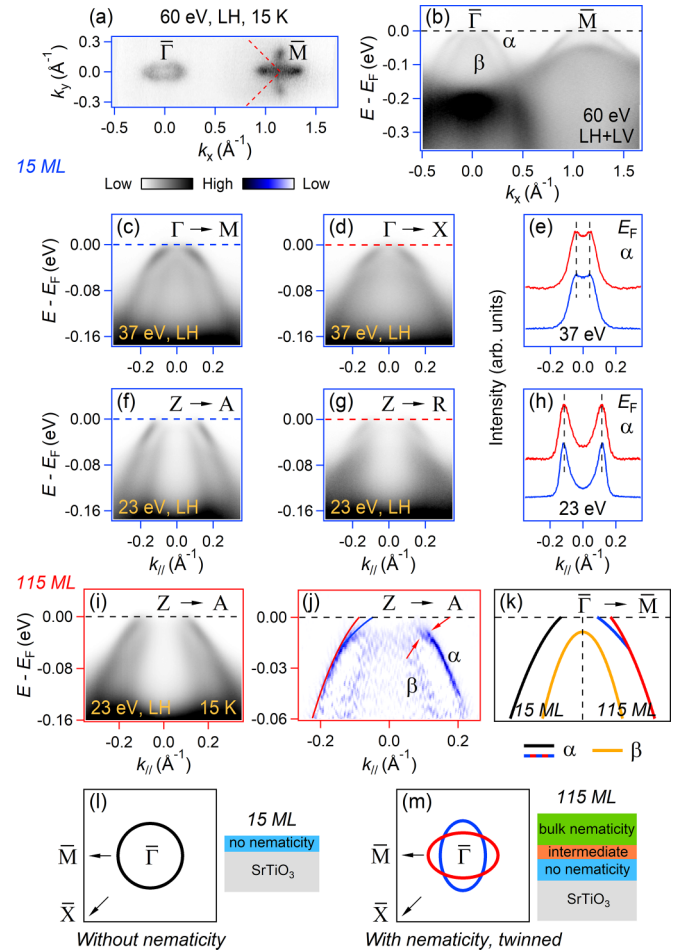

FIG. 3. (a) Intensity plot at E_F [$h\nu = 60$ eV, linear horizontal (LH) polarization] of 15-ML film. (b) Intensity plot measured along the $\bar{\Gamma}$-$\bar{M}$ direction. The intensity is the sum of data acquired with linearly horizontal and vertical polarized photons. [(c),(d)] Intensity plots ($h\nu = 37$ eV, LH polarization, $k_z = 0$) recorded along the Γ-M and Γ-X directions, respectively. (e) MDCs of [(c),(d)] taken at E_F. [(f)–(h)] Same as [(c)–(e)] measured in the $k_z = \pi$ plane ($h\nu = 23$ eV). (i) Same as (f) of 115-ML film. (j) Curvature intensity plot of (i). Red arrows indicate the splitting of α band. (k) Band structure cartoons of 15- and 115-ML films along the $\bar{\Gamma}$-$\bar{M}$ directions at low temperatures. (l) Schematic low-temperature FS around $\bar{\Gamma}$ of single-domained FeSe without nematicity (15-ML film). (m) Same as (l) of twinned FeSe with nematicity (115-ML film). Insets of (l) and (m) show the schematic illustrations of 15- and 115-ML films, respectively.
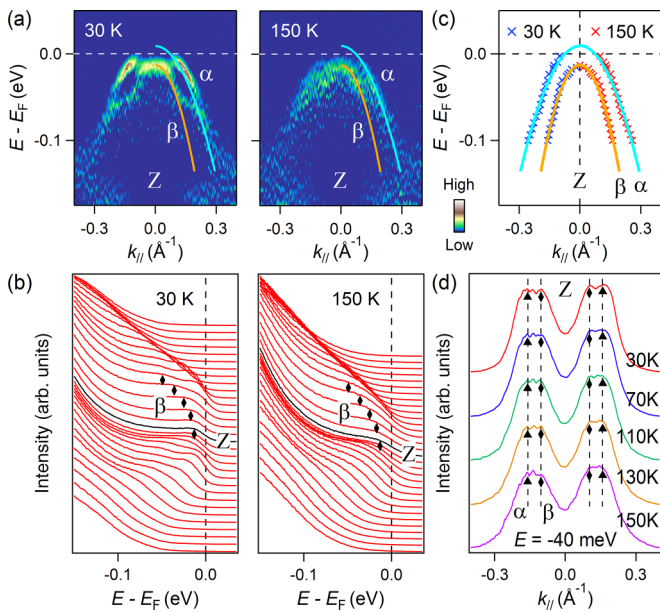
FIG. 4. (a) EDC curvature intensity plots ($h\nu = 23$ eV, LH polarization) taken on 15-ML film along the Z-A direction at 30 and 150 K. (b) Respective EDCs of raw data ($-0.40 < k_\parallel < 0.40$ Å^{-1}). Diamond markers indicate the β bands. (c) Extracted dispersions of α and β bands at 30 and 150 K from EDCs and MDCs together. Solid curves are the parabolic fittings, which are also superimposed on (a). (d) Temperature dependent MDCs taken at -40 meV. Triangle and diamond markers indicate the α and β bands, respectively.

is lowered, with reduced splitting of the α band. It is expected that the outer hole pocket would evolve into an isotropic circular FS when nematicity is quenched in FeSe$_{1-x}$S$_x$. Therefore, we suggest that nematicity is absent in 15-ML film, consistent with the tetragonal lattice symmetry therein.

As discussed above, the bulk region of thick FeSe films is composed of nematicity-related twinned domains. In Fig. 3(i), we measure the near-E_F band structure of 115-ML film under the same conditions as in Fig. 3(f). To facilitate the visualization of dispersive features, we present the two-dimensional curvature analysis [72] of the raw ARPES intensity in Fig. 3(j). As indicated by the red arrows, the splitting of α band is clearly observed; its splitting energy scale of $\sim$20 meV (Fig. 9) is comparable with that in twinned FeSe crystals [26]. The presence of bulklike nematicity in the bulk region of 115-ML film is compatible with the twinned domains therein. To illustrate the contrast between 15- and 115-ML films, we sketch their low-temperature band dispersions along the $\bar{\Gamma}$-$\bar{M}$ directions in Fig. 3(k), the corresponding FSs around $\bar{\Gamma}$ are shown in Figs. 3(l) and 3(m).

To further support the absence of nematicity in 15-ML film, we study the splitting of d_{xz} and d_{yz} orbitals at $\bar{\Gamma}$, the anisotropy between which has been suggested as a hallmark of nematicity [20,21]. As shown in Figs. 4 and 10, we record the band structure of 15-ML film around Z at different temperatures. Upon warming, the β band with band top at ~ -13 meV exhibits little change, as illustrated by the curvature intensity plots and energy distribution curves (EDCs) [Figs. 4(a), 4(b), and 10]. The α band is also less temperature sensitive, as evidenced by the nearly constant

momentum values from the MDCs [Fig. 4(d)], which are taken at -40 meV to avoid the influence of thermal population effect. In Fig. 4(c), by parabolic fits to raw data at 30 and 150 K, we estimate the d_{xz}/d_{yz} splitting as $\sim$22 meV for both temperatures, which is comparable with the spin-orbit-coupling-induced gap ($\sim$20 meV) determined in FeSe [48,66]. The temperature-independent splitting dominated by spin-orbit coupling effect in 15-ML film is distinct from the 115-ML film, where the temperature evolutions of the α and β bands are clearly revealed (Fig. 11).

VI. DISCUSSION

Our observations clearly demonstrate the absence of nematicity induced by the near-interface tensile strain, solving the aforementioned controversy about the nematicity in multilayer FeSe/SrTiO$_3$ films [34,49–52]. The strain effect has been found to exhibit exponential-like relaxation with increasing FeSe thickness [34]. The nematicity strength is therefore expected to gradually recover towards the bulk value between the region without nematicity and the region with bulklike nematicity; namely, an intermediate region probably exists. Overall, as illustrated in Fig. 12 [also the insets of Figs. 3(l) and 3(m)], we suggest that there are likely three regions. In Appendix K, we make an estimate of their spatial scales. Given that the volume of intermediate region is less than 10% of the bulk region, the NMR lines with tiny intensities from the intermediate region could be hidden by the intense f_1-f_2 line.

Last but not least, we discuss the implications of our results for the relationship between nematicity and superconductivity. Extensive studies have been performed to uncover their interplay in FeSe crystals, but the findings are multifarious as described above, leaving it still rather mysterious. The absence of a superconducting gap for undoped multilayer (2–20 MLs) FeSe/SrTiO$_3$ films has been reported in previous STM studies [33,73,74]. Within this thickness range, the nematicity is not present either, based on our results. The simultaneous disappearance of nematicity and superconductivity in thinner FeSe films unambiguously suggests that the suppression of superconductivity therein is not directly related to the nematicity.

VII. CONCLUSION

In summary, we have provided compelling evidence for the suppression of nematicity near the interface of multilayer FeSe/SrTiO$_3$ films. In the bulk region further away from the interface, where the SrTiO$_3$-induced tensile strain is fully relaxed, bulklike nematicity is revealed. The present results facilitate further understanding of the nematicity and its interplay with superconductivity in multilayer FeSe films.

APPENDIX A: NMR MEASUREMENTS OF THE Se-ETCHED SrTiO$_3$ SUBSTRATE

In the frequency-swept ^{77}Se NMR spectra at $T = 40$ K [green curve in Fig. 2(a)], a prominent line ($\sim$113.85 MHz) and a much weaker signal ($\sim$114.06 MHz) are revealed for $H \parallel [100]$. The former shifts to lower frequencies upon cooling while the latter is not observed below 40 K. To distinguish the signal of FeSe film between these two lines, we perform similar measurements at 40 K when there is no sample and a Se-etched SrTiO$_3$ substrate (see Sec. II) [33] on the surface coil, respectively. As shown in Fig. 2(a), first, no visible feature is observed without the sample (purple curve), showing that the aforementioned NMR lines intrinsically come from FeSe/SrTiO$_3$; second, a small hump is observed in the Se-etched SrTiO$_3$ substrate also at $\sim$114.06 MHz (orange curve), like that in the green curve. Therefore, in the green NMR line [Fig. 2(a)], the prominent spectrum at $\sim$113.85 MHz is attributed to the FeSe film; the much weaker signal at $\sim$114.06 MHz is contributed by the Se-etched SrTiO$_3$ substrate, where some of the O atoms might be substituted by Se atoms.

To clarify the reason for the absence of a signal at 114.06 MHz below 40 K in Fig. 2(a), we carry out further measurements on the Se-etched SrTiO$_3$ substrate at 114.06 MHz. In Fig. 5, we present the single FT of the sweep spectra of Se-etched SrTiO$_3$ substrate at 114.06 MHz. At

$T = 40$ K, a small hump is observed as the sweep spectra [orange curve in Fig. 2(a)], while it is not visible at 30 K with the same experimental settings, like the situation below 40 K in Fig. 2(a). We increase the repetition time between the scans from 100 ms (see Appendix B) to 800 ms and measure again at 30 K, but the NMR signal at 114.06 MHz is not much enhanced (green curve in Fig. 5). Then we conduct similar measurements with a repetition time of 100 ms but a lower power of the radio frequency pulses (6 dB, more attenuation). As illustrated in Fig. 5, the signal intensity at 30 K (orange curve) is nearly comparable to that at 40 K (red curve). According to these measurements, we suggest that the absence of the signal at 114.06 MHz below 40 K in Fig. 2(a) could originate from a nonoptimal radio frequency pulse power below 40 K, while this has little effect on the prominent NMR line of the FeSe film. Moreover, the NMR signal from the Se-etched SrTiO$_3$ substrate does not shift with temperature (Fig. 5), further validating the intrinsic origin of the temperature shift of the FeSe NMR signal [Fig. 2(a)].

APPENDIX B: NMR SIGNAL DETECTED IN A LIMITED TEMPERATURE RANGE

We could observe a decent NMR signal only in a limited temperature range between 30 and 40 K. This may have two reasons: (i) the nuclear spin polarization decreases with increasing temperature due to the Boltzmann distribution, so that the NMR signal intensity is proportional to $1/T$ (T is temperature). (ii) The spin-lattice relaxation time (T_1) has a minimum of about 90 ms around 30 K [24]. Each step of the frequency sweep was taken with 160 000 scans, and a repetition time between the scans of 100 ms. A single measurement took almost 4.5 hours, times 13 steps of the frequency sweep, which gives a total measurement time of 58.5 hours for an NMR spectrum at a given temperature. The longer spin-lattice relaxation time T_1 at higher and lower temperatures makes a longer repetition time necessary, and therefore would lead to an even longer total measurement time.

APPENDIX C: DETAILS OF THE FITTING PROCEDURE OF NMR SPECTRA

We carry out the quantitative fit of NMR spectra by using Lorentzian and Gaussian functions respectively. We plot the fitting results in Fig. 6 and summarize the corresponding parameters in Table I. The peak intensity ratio of f_3 to f_2 estimated by Gaussian fitting is slightly bigger than that by Lorentzian fitting. However, as shown in Figs. 6(d)–6(f), the NMR data have not been well reproduced by the Gaussian functions, in contrast to the Lorentzian fitting method [Figs. 6(a)–6(c)]. The Lorentzian function has been generally used in the fit of NMR spectra of various material systems, like FeSe and LaFeAsO [75], NaFe$_{1-x}$Co$_x$As [76], Sr$_2$VFeAsO$_3$ [77], Ca$_{1-x}$La$_x$FeAs$_2$ [78], etc. Therefore, we conclude that each FeSe NMR line consists of three Lorentzian peaks with central frequencies f_1, f_2, and f_3.
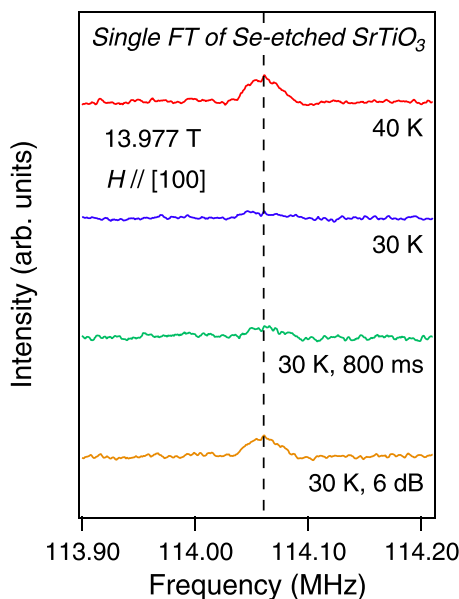

FIG. 5. Single FT of the sweep spectra of Se-etched SrTiO$_3$ substrate at 114.06 MHz. These NMR spectra are recorded with the same experimental settings as the FeSe film, except the green line with a repetition time of 800 ms between the scans and the orange line with a lower radio frequency pulse power of 6 dB.
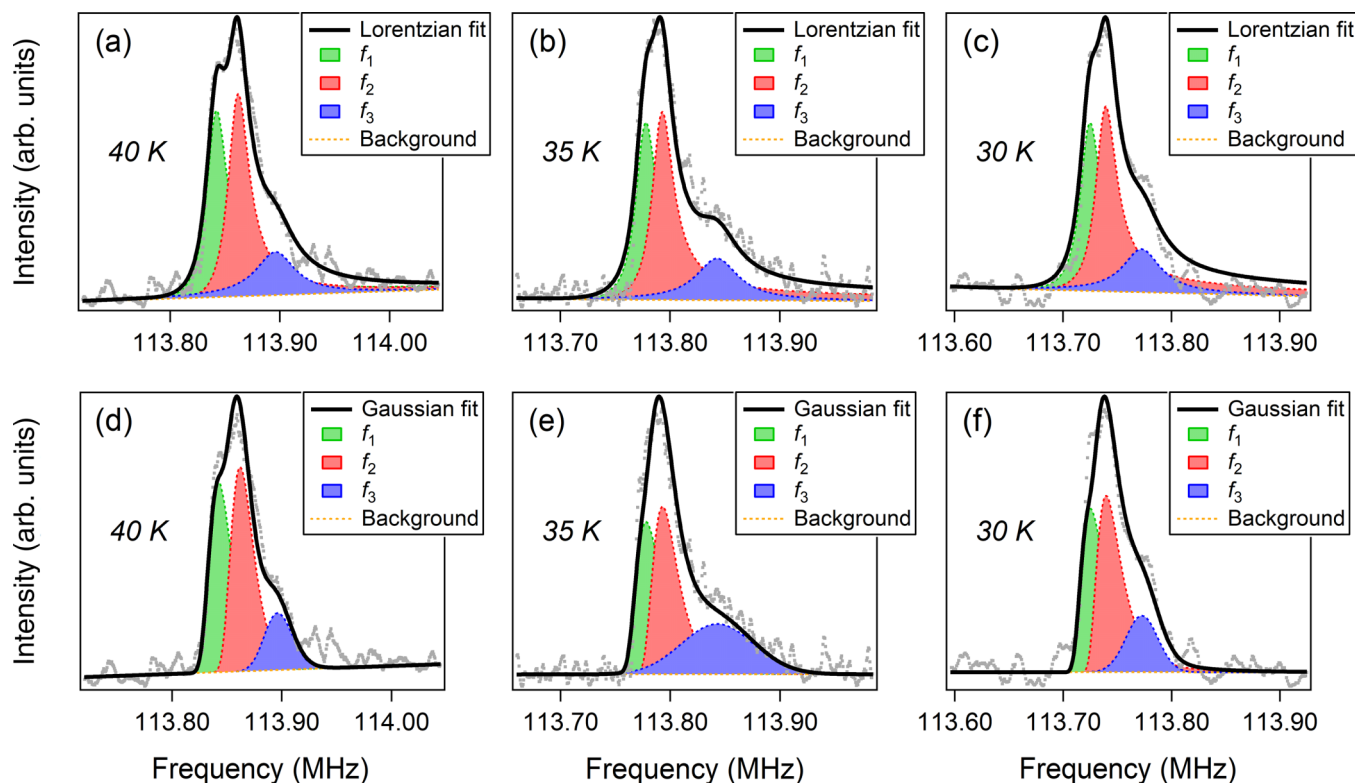
FIG. 6. NMR line-shape fitting by Lorentzian [(a)–(c)] and Gaussian [(d)–(f)] peaks with linear backgrounds (BGs) at three studied temperatures.

APPENDIX D: STRONGER TEMPERATURE DEPENDENCE OF THE KNIGHT SHIFT IN FeSe FILM

Regarding the Knight shift in FeSe film and $FeSe_{0.95}S_{0.05}$ crystal, the order of magnitude of their Knight shift is similar, while the temperature dependence is much stronger in FeSe film in the limited temperature range where we could observe a signal. Since the Knight shift (K) is proportional to the local spin susceptibility (χ_S) through the hyperfine coupling (A_{hf}), some differences in the hyperfine coupling tensor and the spin susceptibility between these two systems are thus expected. Due to the presence of the sizable tensile strain close to the interface of FeSe film, it is clear that the crystallographic structure being different in the crystal and near the $FeSe/SrTiO_3$ interface can make a contribution to their difference related to K_3. But the tensile strain plays a negligible role further away from the interface; the origin of the difference related to K_1-K_2 between crystal and the bulk region of film could thus be more complicated, and still remains elusive.

Here we make a simple estimate of the contributions of the strain effect in their difference related to K_3. In our 210-ML FeSe film, for $T > T_{nem}$, the f_1 and f_2 lines are expected to be degenerate, and the splitting between f_3 and the degenerate f_1, f_2 pair (that is, the splitting of Knight shifts) should be mainly caused by the different crystallographic structures close to and further away from the interface, owing to the substrate-induced tensile strain. Since the strain effect is less temperature sensitive, the splitting between K_3 and the average of K_1, K_2 below T_{nem} should be similar to that above T_{nem}. Therefore, as shown in Fig. 7, the average splitting between K_3 (black solid star) and $K_{1,2}^{ave}$ (red solid circle) at three studied

temperatures can be regarded as the contribution of the strain effect (K^{stra}). After adding K^{stra} to the Knight shifts of crystal (grey solid triangle), the resulting values (black hollow star) noticeably deviate from the evolution trend of K_3, indicating that only the strain effect is not sufficient to explain the enhanced temperature dependence of the Knight shift in FeSe
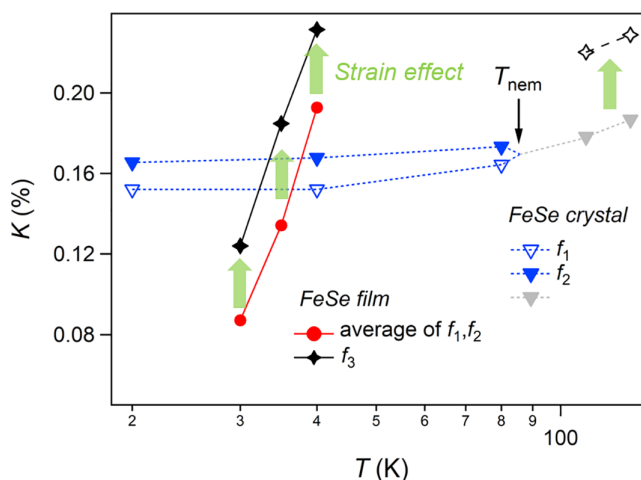

FIG. 7. Temperature dependent ^{77}Se NMR Knight shift of the 210-ML FeSe film and an $FeSe_{0.95}S_{0.05}$ crystal ($H \parallel [100]$), adopted from Fig. 2(c). The strain effect (K^{stra}, indicated by the green arrow) is determined by the average splitting between K_3 and $K_{1,2}^{ave}$ at 30, 35, and 40 K. Black hollow stars indicate the Knight shifts after including the strain effect in the crystal at $T > T_{nem}$.

film, even for K_3. There should exist other potential effects playing more essential roles in determining the Knight shift of FeSe film.

APPENDIX E: CHALLENGE OF DETECTING THE SINGLE-DOMAIN STRUCTURE IN 15-ML FeSe FILM BY NMR

For directly detecting the single-domain structure in the 15-ML film by NMR measurements, we think it is challenging to get decent results currently. As described in Sec. II, we estimated that there are about 2×10^{16} NMR active Se nuclei in the 210-ML FeSe film. The 15-ML film, then, has about 1.4×10^{15} ^{77}Se nuclei, which is about 14 times less than that of the 210-ML film and about 70 times less than that of an FeSe single crystal with typical dimension $1 \times 0.5 \times 0.1$ mm^3. The NMR measurements of the 210-ML film took about 58.5 hours for an NMR spectrum at a given temperature, the signal we recorded was almost at the limit of what could be measured. As a result, for the 15-ML film with such small amounts of ^{77}Se nuclei, it is challenging to obtain a decent NMR intensity and an NMR signal-to-noise ratio comparable to the 210-ML film.

APPENDIX F: DIFFERENCE BETWEEN THE f_3 NMR LINE IN FeSe FILM AND THE PROMINENT NMR PEAK IN DETWINNED FeSe CRYSTAL

Recently, a ^{77}Se NMR study was performed on detwinned FeSe crystals [75]. The sample detwinning was conducted under mechanical uniaxial strain. Upon the detwinning of crystals, the original double-peak splitting associated with the twinned domains at low temperatures evolves into a prominent peak and a nearly quenched one. This prominent NMR line in detwinned FeSe crystals is distinct from the f_3 NMR line observed here in FeSe film. As discussed in Sec. V, although the films near the FeSe/SrTiO$_3$ interface and detwinned FeSe crystals share the similarity of single-domain structure, there is no preferred orientation for the films under the SrTiO$_3$-induced tensile strain, which is distinct from the uniaxial strain mechanically added to the crystals. Thus, the former has tetragonal structure (illustrated by STM of 15-ML film) while the latter shows orthorhombicity.

In detwinned FeSe crystals, the uniaxial strain aligns the twinned orthorhombic domains according to one of them, i.e., along the [100] or [010] direction, thus when the applied field is parallel to the [100] or [010] direction, the nematicity-related in-plane symmetry change cannot be revealed by NMR, resulting in the single NMR peak (the presence of another peak with the much weaker intensity in Ref. [75] could stem from the incomplete detwinning), which is located at one of the frequencies of the original splitting peaks. However, for the region close to the interface of FeSe films, its tetragonal structure is in contrast to the twinned orthorhombic structure of the bulk region of films. Consequently, the peak frequency f_3 associated with the former structure is separated from f_1 and f_2 of the latter structure (Fig. 2). This fact further demonstrates that the single-domain structure near the FeSe/SrTiO$_3$ interface is in marked contrast to that in detwinned FeSe crystals.
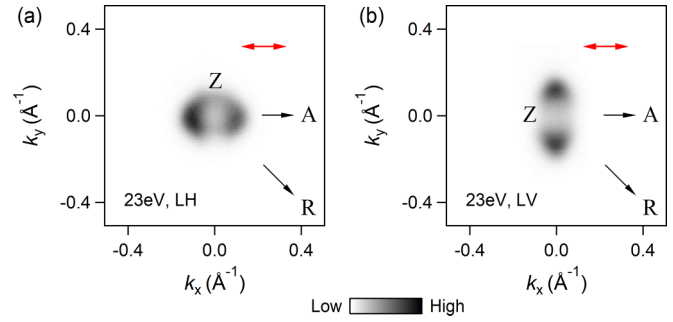

FIG. 8. (a) Constant-energy ARPES image around Z ($h\nu = 23$ eV, LH polarization, $k_z = \pi$) of another 15-ML FeSe film obtained by integrating the photoemission intensity within $E_F \pm 20$ meV. (b) Same as (a) recorded at $h\nu = 23$ eV ($k_z = \pi$) with LV polarization. The red arrows in [(a),(b)] indicate that the analyzer slit is parallel to the [110] direction.

APPENDIX G: PHOTON POLARIZATION DEPENDENCE OF THE HOLE POCKET AROUND Z IN 15-ML FeSe FILM

The FS topology in Fig. 3(a) shows an ellipselike hole pocket at $\bar{\Gamma}$, which seems to be similar to that in detwinned FeSe crystals (detwinned by the mechanical uniaxial strain) below T_{nem} [45,47,67,68]. However, the single-domain structure of 15-ML FeSe film is in marked contrast to that of detwinned FeSe crystals, which could strongly differentiate their electronic structure. To demonstrate that the FS around $\bar{\Gamma}$ of 15-ML film is distinct from that in detwinned FeSe crystals, we further record the FS around Z ($h\nu = 23$ eV, $k_z = \pi$, $T = 15$ K) on another 15-ML film using photons with LH and linear vertical (LV) polarizations. As shown in Fig. 8, the elongation of the ellipselike FS varies from $k_y = 0$ line [Fig. 8(a)] to $k_x = 0$ line [Fig. 8(b)] when switching the incident photons from LH to LV polarizations. This evolution clearly distinguishes the FS around $\bar{\Gamma}$ in 15-ML FeSe film from that in detwinned FeSe crystals, where the elongation of the ellipselike hole pocket is perpendicular to the strain direction regardless of the incident beam polarization [47,68].
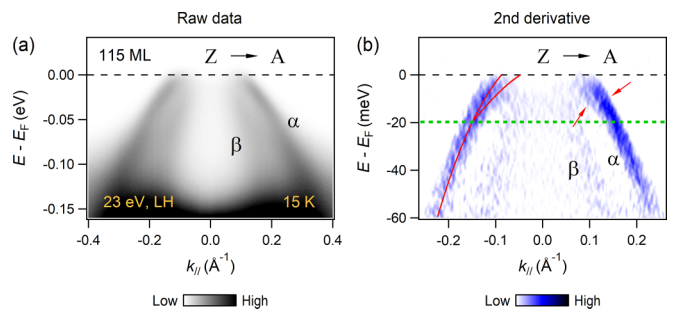

FIG. 9. (a) ARPES intensity plot ($h\nu = 23$ eV, LH polarization, $k_z = \pi$, $T = 15$ K) of the 115-ML FeSe film recorded along the $\bar{\Gamma}$-$\bar{M}$ direction. (b) Second derivative intensity plot of (a). Red arrows indicate the splitting of the α band at Z. Red solid curves are guides to the eye, determined according to the right branch of the split α band. The green dashed line indicates the energy scale ($\sim$20 meV) of the band splitting.
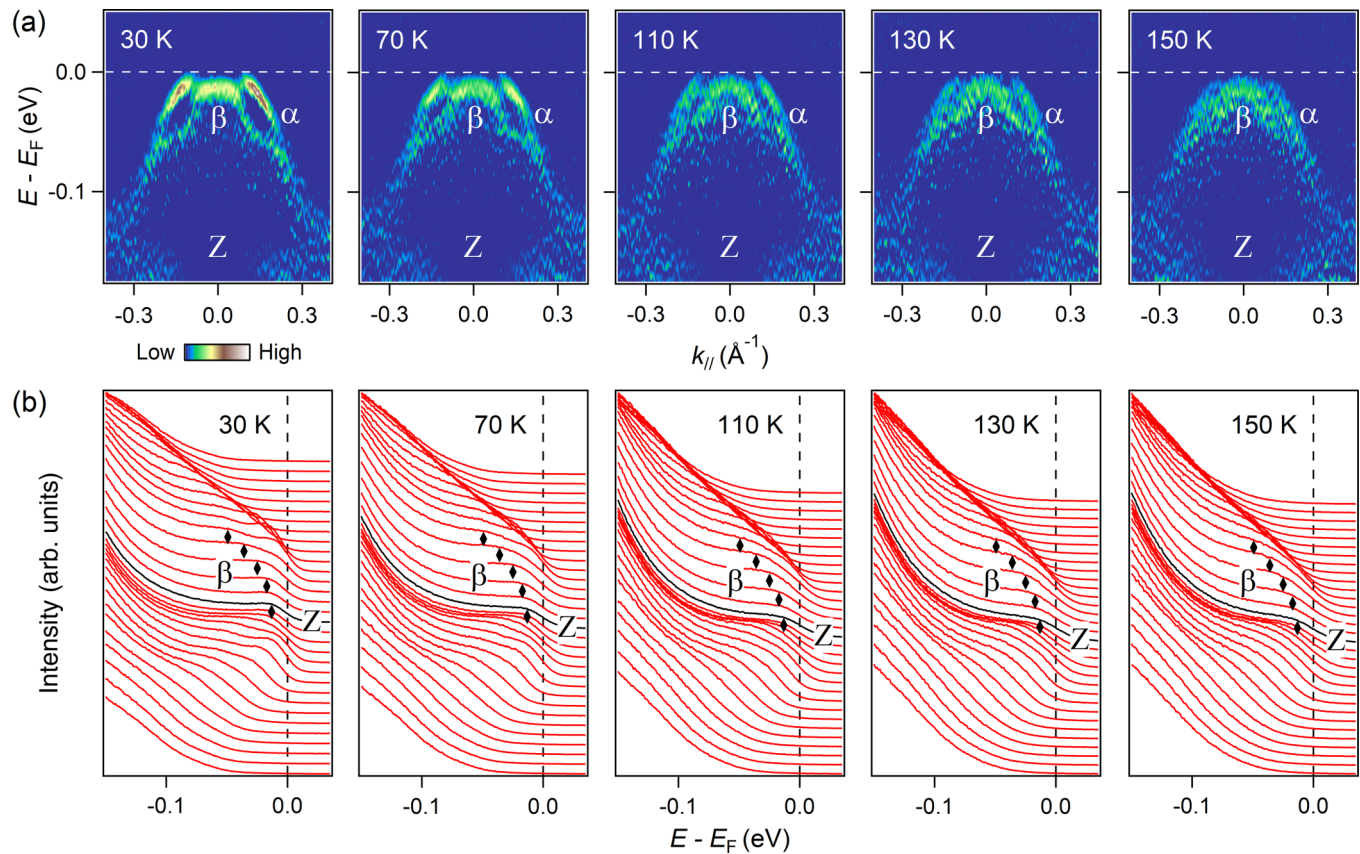
FIG. 10. (a) EDC curvature intensity plots ($h\nu = 23$ eV, LH polarization, $k_z = \pi$) taken on the 15-ML FeSe film along the Z-A direction at different temperatures. (b) Respective EDC plots of raw data at different temperatures over the momentum range of $-0.40 < k_{\parallel} < 0.40$ Å^{-1}. The diamond markers indicate the β bands around Z.

APPENDIX H: SPLITTING ENERGY SCALE OF THE α BAND IN 115-ML FeSe FILM

To further demonstrate that the nematicity could recover in the bulk region of thick FeSe films, we fabricated

115-ML FeSe film and performed ARPES measurements on it. Since the hole pocket at zone center of $k_z = \pi$ plane is larger than that of $k_z = 0$ plane, to visualize the splitting of the outer hole band α around $\bar{\Gamma}$ and to avoid the possible influence of the branch in opposite momentum, the near-E_F band
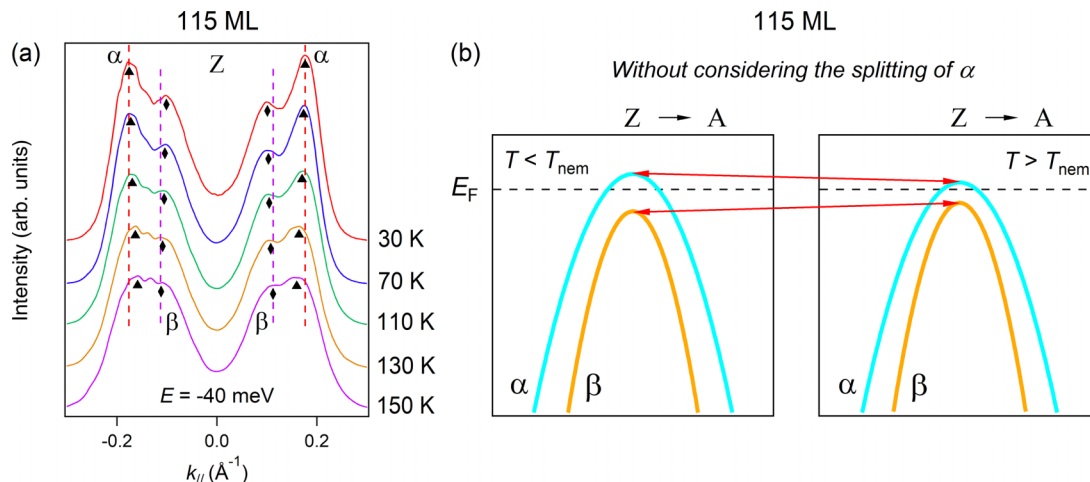

FIG. 11. (a) Temperature dependent MDCs of the 115-ML FeSe film taken at -40 meV. Triangle and diamond markers indicate the α and β bands around Z, respectively. Red and purple dashed lines show the peak positions of α and β at 30 and 150 K, respectively. (b) Band structure diagrams of the 115-ML FeSe film along the Z-A direction below and above T_{nem}. The splitting of α band below T_{nem} is not considered here for better visualization of the band shifts.

structure along the $\bar{\Gamma}$-$\bar{M}$ direction is measured in the $k_z = \pi$ plane ($h\nu = 23$ eV). As shown in Fig. 9(b), the splitting of the α band is revealed, especially at the right branch, indicated by the red arrows. Its splitting energy scale of ~ 20 meV [indicated by the green dashed line in Fig. 9(b)] is comparable with that in twinned FeSe crystals [26]. We then carry out the two-dimensional curvature analysis of the raw ARPES intensity plot [72]. As shown in Fig. 3(j), the band splitting is illustrated more clearly. These observations are in sharp contrast to the 15-ML film, showing the presence of bulk-like nematicity in the bulk region of the 115-ML film.

APPENDIX I: TEMPERATURE DEPENDENCE OF THE NEAR-E_F BAND STRUCTURE AROUND Z IN 15-ML FeSe FILM

To study the temperature dependence of d_{xz}/d_{yz} splitting around $\bar{\Gamma}$ in 15-ML FeSe film, we measure the near-E_F band structure along the *Z-A* direction ($h\nu = 23$ eV, $k_z = \pi$) at different temperatures using LH-polarized photons. In Fig. 10(a), we present the EDC curvatures of raw data to better visualize the binding energy associated with the top of inner hole band β. Upon warming up the film from 30 to 150 K, one can obtain that the β band shows little change with its band top ~ 13 meV below E_F, as further evidenced by the EDC plots (traced out by the diamond markers) in Fig. 10(b). The temperature independence of the outer hole band α is illustrated by the nearly constant momentum values from the MDCs in Fig. 4(d). Therefore, we conclude that the d_{xz}/d_{yz} splitting at $\bar{\Gamma}$ is less temperature sensitive in 15-ML FeSe film.

APPENDIX J: TEMPERATURE EVOLUTIONS OF THE α AND β BANDS IN 115-ML FeSe FILM

We then measure the band structure of 115-ML FeSe film along the *Z-A* direction at different temperatures. As shown in Fig. 11(a), the temperature evolutions of the α and β bands can be clearly revealed from their evolving momentum values in the MDCs, which are taken at -40 meV to avoid the influence of thermal population effect. Upon warming, the monotonic decrease (increase) of the momentum value of α (β) band indicates the downward (upward) band shift, as schematically illustrated in Fig. 11(b). The temperature evolutions demonstrate an extra splitting between α and β bands at low temperatures associated with a d_{xz}/d_{yz} orbital
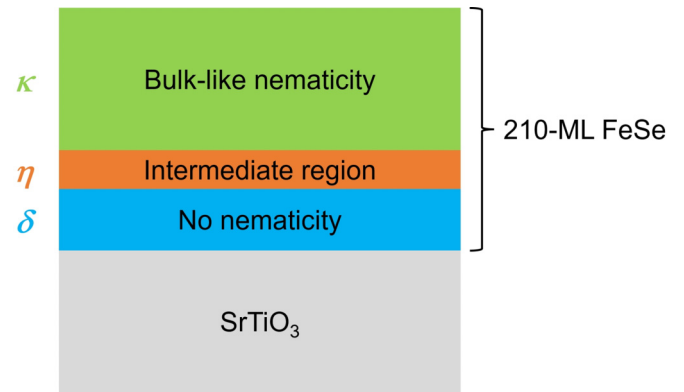

FIG. 12. Schematic illustration of the 210-ML FeSe film with three regions, whose respective thicknesses are denoted as δ, η, and κ.

polarization, in addition to the spin-orbit-coupling-induced gap between them at high temperatures. This observation further validates the existence of nematicity in the bulk region of 115-ML FeSe film.

APPENDIX K: AN ESTIMATE OF THE SPATIAL SCALES OF THE NON-NEMATIC AND INTERMEDIATE REGIONS

Although it is challenging to directly determine the spatial scales of the non-nematic and intermediate regions, we can make an estimate by considering both the current results and earlier data in the literature. As schematically shown in Fig. 12, we assign the numbers of layers for these three regions as δ, η, and κ, respectively. Based on the Lorentzian fitting results of the NMR spectra in Appendix C, the average of the peak intensity ratios $f_3/(f_2 + f_3)$ (or f_3/f_2) at three studied temperatures is 18% (or 22%). This value from the NMR data can be regarded as the volume proportion between the regions, i.e., $\delta/(\delta + \kappa) \times 100\% = 18\%$ (or $\delta/\kappa \times 100\% = 22\%$). It has been reported that the lattice constant of FeSe films reaches the bulk value of 3.76 Å at ~ 50 MLs [34]. Thus, one can obtain $\delta \sim 35$ MLs and $\eta \sim 15$ MLs by using $\kappa \sim 160$ MLs. Although the estimated spatial scales of the non-nematic and intermediate regions could have some uncertainties, it is clear that our NMR data provide essential information for identifying these three regions.

[1] S. A. Kivelson, E. Fradkin, and V. J. Emery, Electronic liquid-crystal phases of a doped Mott insulator, Nature (London) **393**, 550 (1998).

[2] Y. Ando, K. Segawa, S. Komiya, and A. N. Lavrov, Electrical resistivity anisotropy from self-organized one dimensionality in high-temperature superconductors, Phys. Rev. Lett. **88**, 137005 (2002).

[3] R. Daou, J. Chang, D. LeBoeuf, O. Cyr-Choinière, F. Laliberté, N. Doiron-Leyraud, B. J. Ramshaw, R. Liang, D. A. Bonn, W. N. Hardy, and L. Taillefer, Broken rotational symmetry in the pseudogap phase of a high-T_c superconductor, Nature (London) **463**, 519 (2010).

[4] M. J. Lawler, K. Fujita, J. Lee, A. R. Schmidt, Y. Kohsaka, C. K. Kim, H. Eisaki, S. Uchida, J. C. Davis, J. P. Sethna, and E.-A. Kim, Intra-unit-cell electronic nematicity of the high-T_c copper-oxide pseudogap states, Nature (London) **466**, 347 (2010).

[5] J. Wu, A. T. Bollinger, X. He, and I. Božović, Spontaneous breaking of rotational symmetry in copper oxide superconductors, Nature (London) **547**, 432 (2017).

[6] T.-M. Chuang, M. P. Allan, J. Lee, Y. Xie, N. Ni, S. L. Bud'ko, G. S. Boebinger, P. C. Canfield, and J. C. Davis, Nematire in the "parent" state of the iron-based superconductor Ca(Fe$_{1-x}$Co$_x$)$_2$As$_2$, Science **327**, 181 (2010).

[7] J.-H. Chu, J. G. Analytis, K. D. Greve, P. L. McMahon, Z. Islam, Y. Yamamoto, and I. R. Fisher, In-plane resistivity anisotropy in an underdoped iron arsenide superconductor, Science **329**, 824 (2010).

[8] J.-H. Chu, H.-H. Kuo, J. G. Analytis, and I. R. Fisher, Divergent nematic susceptibility in an iron arsenide superconductor, Science **337**, 710 (2012).

[9] H.-H. Kuo, J.-H. Chu, J. C. Palmstrom, S. A. Kivelson, and I. R. Fisher, Ubiquitous signatures of nematic quantum criticality in optimally doped Fe-based superconductors, Science **352**, 958 (2016).

[10] M. Yi, D. Lu, J.-H. Chu, J. G. Analytis, A. P. Sorini, A. F. Kemper, B. Moritz, S.-K. Mo, R. G. Moore, M. Hashimoto, W.-S. Lee, Z. Hussain, T. P. Devereaux, I. R. Fisher, and Z.-X. Shen, Symmetry-breaking orbital anisotropy observed for detwinned $Ba(Fe_{1-x}Co_x)_2As_2$ above the spin density wave transition, Proc. Natl. Acad. Sci. USA **108**, 6878 (2011).

[11] Y. Zhang, C. He, Z. R. Ye, J. Jiang, F. Chen, M. Xu, Q. Q. Ge, B. P. Xie, J. Wei, M. Aeschlimann, X. Y. Cui, M. Shi, J. P. Hu, and D. L. Feng, Symmetry breaking via orbital-dependent reconstruction of electronic structure in detwinned NaFeAs, Phys. Rev. B **85**, 085121 (2012).

[12] R. M. Fernandes, A. V. Chubukov, and J. Schmalian, What drives nematic order in iron-based superconductors? Nat. Phys. **10**, 97 (2014).

[13] D. C. Johnston, The puzzle of high temperature superconductivity in layered iron pnictides and chalcogenides, Adv. Phys. **59**, 803 (2010).

[14] C. de la Cruz, Q. Huang, J. W. Lynn, J. Li, W. Ratcliff II, J. L. Zarestky, H. A. Mook, G. F. Chen, J. L. Luo, N. L. Wang, and P. Dai, Magnetic order close to superconductivity in the iron-based layered $LaO_{1-x}F_xFeAs$ systems, Nature (London) **453**, 899 (2008).

[15] J. Zhao, Q. Huang, C. de la Cruz, S. Li, J. W. Lynn, Y. Chen, M. A. Green, G. F. Chen, G. Li, Z. Li, J. L. Luo, N. L. Wang, and P. Dai, Structural and magnetic phase diagram of $CeFeAsO_{1-x}F_x$ and its relation to high-temperature superconductivity, Nat. Mater. **7**, 953 (2008).

[16] S. Kasahara, H. J. Shi, K. Hashimoto, S. Tonegawa, Y. Mizukami, T. Shibauchi, K. Sugimoto, T. Fukuda, T. Terashima, A. H. Nevidomskyy, and Y. Matsuda, Electronic nematicity above the structural and superconducting transition in $BaFe_2(As_{1-x}P_x)_2$, Nature (London) **486**, 382 (2012).

[17] X. Lu, J. T. Park, R. Zhang, H. Luo, A. H. Nevidomskyy, Q. Si, and P. Dai, Nematic spin correlations in the tetragonal state of uniaxial-strained $BaFe_{2-x}Ni_xAs_2$, Science **345**, 657 (2014).

[18] C. Fang, H. Yao, W.-F. Tsai, J. P. Hu, and S. A. Kivelson, Theory of electron nematic order in LaFeAsO, Phys. Rev. B **77**, 224509 (2008).

[19] C. Xu, M. Müller, and S. Sachdev, Ising and spin orders in the iron-based superconductors, Phys. Rev. B **78**, 020501(R) (2008).

[20] C.-C. Lee, W.-G. Yin, and W. Ku, Ferro-orbital order and strong magnetic anisotropy in the parent compounds of iron-pnictide superconductors, Phys. Rev. Lett. **103**, 267001 (2009).

[21] C.-C. Chen, J. Maciejko, A. P. Sorini, B. Moritz, R. R. P. Singh, and T. P. Devereaux, Orbital order and spontaneous orthorhombicity in iron pnictides, Phys. Rev. B **82**, 100504(R) (2010).

[22] T. M. McQueen, A. J. Williams, P. W. Stephens, J. Tao, Y. Zhu, V. Ksenofontov, F. Casper, C. Felser, and R. J. Cava, Tetragonal-to-orthorhombic structural phase transition at 90 K in the superconductor $Fe_{1.01}Se$, Phys. Rev. Lett. **103**, 057002 (2009).

[23] S. Medvedev, T. M. McQueen, I. A. Troyan, T. Palasyuk, M. I. Eremets, R. J. Cava, S. Naghavi, F. Casper, V. Ksenofontov, G. Wortmann, and C. Felser, Electronic and magnetic phase diagram of β-$Fe_{1.01}Se$ with superconductivity at 36.7 K under pressure, Nat. Mater. **8**, 630 (2009).

[24] S.-H. Baek, D. V. Efremov, J. M. Ok, J. S. Kim, J. van den Brink, and B. Büchner, Orbital-driven nematicity in FeSe, Nat. Mater. **14**, 210 (2015).

[25] K. Nakayama, Y. Miyata, G. N. Phan, T. Sato, Y. Tanabe, T. Urata, K. Tanigaki, and T. Takahashi, Reconstruction of band structure induced by electronic nematicity in an FeSe superconductor, Phys. Rev. Lett. **113**, 237001 (2014).

[26] M. D. Watson, T. K. Kim, A. A. Haghighirad, N. R. Davies, A. McCollam, A. Narayanan, S. F. Blake, Y. L. Chen, S. Ghannadzadeh, A. J. Schofield, M. Hoesch, C. Meingast, T. Wolf, and A. I. Coldea, Emergence of the nematic electronic state in FeSe, Phys. Rev. B **91**, 155106 (2015).

[27] A. E. Böhmer, T. Arai, F. Hardy, T. Hattori, T. Iye, T. Wolf, H. V. Löhneysen, K. Ishida, and C. Meingast, Origin of the tetragonal-to-orthorhombic phase transition in FeSe: A combined thermodynamic and NMR study of nematicity, Phys. Rev. Lett. **114**, 027001 (2015).

[28] J. Guo, S. Jin, G. Wang, S. Wang, K. Zhu, T. Zhou, M. He, and X. Chen, Superconductivity in the iron selenide $K_xFe_2Se_2$ $(0 \leqslant x \leqslant 1.0)$, Phys. Rev. B **82**, 180520(R) (2010).

[29] X. F. Lu, N. Z. Wang, H. Wu, Y. P. Wu, D. Zhao, X. Z. Zeng, X. G. Luo, T. Wu, W. Bao, G. H. Zhang, F. Q. Huang, Q. Z. Huang, and X. H. Chen, Coexistence of superconductivity and antiferromagnetism in $(Li_{0.8}Fe_{0.2})OHFeSe$, Nat. Mater. **14**, 325 (2015).

[30] X. Dong, K. Jin, D. Yuan, H. Zhou, J. Yuan, Y. Huang, W. Hua, J. Sun, P. Zheng, W. Hu, Y. Mao, M. Ma, G. Zhang, F. Zhou, and Z. Zhao, $(Li_{0.84}Fe_{0.16})OHFe_{0.98}Se$ superconductor: Ion-exchange synthesis of large single-crystal and highly two-dimensional electron properties, Phys. Rev. B **92**, 064515 (2015).

[31] X. Dong, H. Zhou, H. Yang, J. Yuan, K. Jin, F. Zhou, D. Yuan, L. Wei, J. Li, X. Wang, G. Zhang, and Z. Zhao, Phase diagram of $(Li_{1-x}Fe_x)OHFeSe$: A bridge between iron selenide and arsenide superconductors, J. Am. Chem. Soc. **137**, 66 (2015).

[32] P. Shahi, J. P. Sun, S. H. Wang, Y. Y. Jiao, K. Y. Chen, S. S. Sun, H. C. Lei, Y. Uwatoko, B. S. Wang, and J.-G. Cheng, High-T_c superconductivity up to 55 K under high pressure in a heavily electron doped $Li_{0.36}(NH_3)_yFe_2Se_2$ single crystal, Phys. Rev. B **97**, 020508(R) (2018).

[33] Q.-Y. Wang, Z. Li, W.-H. Zhang, Z.-C. Zhang, J.-S. Zhang, W. Li, H. Ding, Y.-B. Ou, P. Deng, K. Chang, J. Wen, C.-L. Song, K. He, J.-F. Jia, S.-H. Ji, Y.-Y. Wang, L.-L. Wang, X. Chen, X.-C. Ma, and Q.-K. Xue, Interface-induced high-temperature superconductivity in single unit-cell FeSe films on $SrTiO_3$, Chin. Phys. Lett. **29**, 037402 (2012).

[34] S. Tan, Y. Zhang, M. Xia, Z. Ye, F. Chen, X. Xie, R. Peng, D. Xu, Q. Fan, H. Xu, J. Jiang, T. Zhang, X. Lai, T. Xiang, J. Hu, B. Xie, and D. L. Feng, Interface-induced superconductivity and strain-dependent spin density waves in $FeSe/SrTiO_3$ thin films, Nat. Mater. **12**, 634 (2013).

[35] S. He, J. He, W. Zhang, L. Zhao, D. Liu, X. Liu, D. Mou, Y. Ou, Q. Wang, Z. Li, L. Wang, Y. Peng, Y. Liu, C. Chen, L. Yu, G. Liu, X. Dong, J. Zhang, C. Chen, Z. Xu, X. Chen, X. Ma, Q.-K. Xue, and X. J. Zhou, Phase diagram and electronic indication of high-temperature superconductivity at 65 K in single-layer FeSe films, Nat. Mater. **12**, 605 (2013).

[36] J.-F. Ge, Z. Liu, C. Liu, C. Gao, D. Qian, Q.-K. Xue, Y. Liu, and J.-F. Jia, Superconductivity above 100 K in single-layer FeSe films on doped SrTiO₃, Nat. Mater. **14**, 285 (2015).

[37] S. Teknowijoyo, K. Cho, M. A. Tanatar, J. Gonzales, A. E. Böhmer, O. Cavani, V. Mishra, P. J. Hirschfeld, S. L. Bud'ko, P. C. Canfield, and R. Prozorov, Enhancement of superconducting transition temperature by pointlike disorder and anisotropic energy gap in FeSe single crystals, Phys. Rev. B **94**, 064521 (2016).

[38] P. S. Wang, S. S. Sun, Y. Cui, W. H. Song, T. R. Li, R. Yu, H. C. Lei, and W. Yu, Pressure induced stripe-order antiferromagnetism and first-order phase transition in FeSe, Phys. Rev. Lett. **117**, 237001 (2016).

[39] M. Ghini, M. Bristow, J. C. A. Prentice, S. Sutherland, S. Sanna, A. A. Haghighirad, and A. I. Coldea, Strain tuning of nematicity and superconductivity in single crystals of FeSe, Phys. Rev. B **103**, 205139 (2021).

[40] J. M. Bartlett, A. Steppke, S. Hosoi, H. Noad, J. Park, C. Timm, T. Shibauchi, A. P. Mackenzie, and C. W. Hicks, Relationship between transport anisotropy and nematicity in FeSe, Phys. Rev. X **11**, 021038 (2021).

[41] L. Wang, F. Hardy, T. Wolf, P. Adelmann, R. Fromknecht, P. Schweiss, and C. Meingast, Superconductivity-enhanced nematicity and "$s + d$" gap symmetry in Fe(Se$_{1-x}$S$_x$), Phys. Status Solidi B **254**, 1600153 (2017).

[42] A. E. Böhmer, F. Hardy, F. Eilers, D. Ernst, P. Adelmann, P. Schweiss, T. Wolf, and C. Meingast, Lack of coupling between superconductivity and orthorhombic distortion in stoichiometric single-crystalline FeSe, Phys. Rev. B **87**, 180505(R) (2013).

[43] P. Zhang, T. Qian, P. Richard, X. P. Wang, H. Miao, B. Q. Lv, B. B. Fu, T. Wolf, C. Meingast, X. X. Wu, Z. Q. Wang, J. P. Hu, and H. Ding, Observation of two distinct d_{xz}/d_{yz} band splittings in FeSe, Phys. Rev. B **91**, 214503 (2015).

[44] T. Shimojima, Y. Suzuki, T. Sonobe, A. Nakamura, M. Sakano, J. Omachi, K. Yoshioka, M. Kuwata-Gonokami, K. Ono, H. Kumigashira, A. E. Böhmer, F. Hardy, T. Wolf, C. Meingast, H. v. Löhneysen, H. Ikeda, and K. Ishizaka, Lifting of xz/yz orbital degeneracy at the structural transition in detwinned FeSe, Phys. Rev. B **90**, 121111(R) (2014).

[45] M. Yi, H. Pfau, Y. Zhang, Y. He, H. Wu, T. Chen, Z. R. Ye, M. Hashimoto, R. Yu, Q. Si, D.-H. Lee, P. Dai, Z.-X. Shen, D. H. Lu, and R. J. Birgeneau, Nematic energy scale and the missing electron pocket in FeSe, Phys. Rev. X **9**, 041049 (2019).

[46] M. D. Watson, T. K. Kim, L. C. Rhodes, M. Eschrig, M. Hoesch, A. A. Haghighirad, and A. I. Coldea, Evidence for unidirectional nematic bond ordering in FeSe, Phys. Rev. B **94**, 201107(R) (2016).

[47] M. D. Watson, A. A. Haghighirad, L. C. Rhodes, M. Hoesch, and T. K. Kim, Electronic anisotropies revealed by detwinned angle-resolved photo-emission spectroscopy measurements of FeSe, New J. Phys. **19**, 103021 (2017).

[48] A. Fedorov, A. Yaresko, T. K. Kim, Y. Kushnirenko, E. Haubold, T. Wolf, M. Hoesch, A. Grüneis, B. Büchner, and S. V. Borisenko, Effect of nematic ordering on electronic structure of FeSe, Sci. Rep. **6**, 36834 (2016).

[49] R. Peng, H. C. Xu, and D. L. Feng, In-situ spectroscopic studies and interfacial engineering on FeSe/oxide heterostructures: Insights on the interfacial superconductivity, Chin. Phys. B **24**, 117902 (2015).

[50] C. H. P. Wen, H. C. Xu, C. Chen, Z. C. Huang, X. Lou, Y. J. Pu, Q. Song, B. P. Xie, M. Abdel-Hafiez, D. A. Chareev, A. N. Vasiliev, R. Peng, and D. L. Feng, Anomalous correlation effects and unique phase diagram of electron-doped FeSe revealed by photoemission spectroscopy, Nat. Commun. **7**, 10840 (2016).

[51] G. N. Phan, K. Nakayama, K. Sugawara, T. Sato, T. Urata, Y. Tanabe, K. Tanigaki, F. Nabeshima, Y. Imai, A. Maeda, and T. Takahashi, Effects of strain on the electronic structure, superconductivity, and nematicity in FeSe studied by angle-resolved photoemission spectroscopy, Phys. Rev. B **95**, 224507 (2017).

[52] D. Liu, L. Zhao, S. He, Y. Hu, B. Shen, J. Huang, A. Liang, Y. Xu, X. Liu, J. He, D. Mou, S. Liu, H. Liu, G. Liu, W. Zhang, F. Li, X. C. Ma, Q.-K. Xue, X. H. Chen, G. F. Chen, L. Yu, J. Zhang, Z. Y. Xu, C. T. Chen, and X. J. Zhou, Common electronic features and electronic nematicity in parent compounds of iron-based superconductors and FeSe/SrTiO₃ films revealed by angle-resolved photoemission spectroscopy, Chin. Phys. Lett. **33**, 077402 (2016).

[53] A. I. Coldea and M. D. Watson, The key ingredients of the electronic structure of FeSe, Annu. Rev. Condens. Matter Phys. **9**, 125 (2018).

[54] A. Varykhalov, O. Rader, and W. Gudat, Structure and quantum-size effects in a surface carbide: W(110)/C-*R*(15 × 3), Phys. Rev. B **72**, 115440 (2005).

[55] W. Liu, L. Lu, and V. F. Mitrović, Application of surface coil in nuclear magnetic resonance studies of physical properties of quasi-2D materials, Rev. Sci. Instrum. **88**, 113902 (2017).

[56] S.-H. Baek, J. M. Ok, J. S. Kim, S. Aswartham, I. Morozov, D. Chareev, T. Urata, K. Tanigaki, Y. Tanabe, B. Büchner, and D. V. Efremov, Separate tuning of nematicity and spin fluctuations to unravel the origin of superconductivity in FeSe, npj Quantum Mater. **5**, 8 (2020).

[57] J. Li, B. Lei, D. Zhao, L. P. Nie, D. W. Song, L. X. Zheng, S. J. Li, B. L. Kang, X. G. Luo, T. Wu, and X. H. Chen, Spin-orbital-intertwined nematic state in FeSe, Phys. Rev. X **10**, 011034 (2020).

[58] S. Molatta, D. Opherden, J. Wosnitza, L. Opherden, Z. T. Zhang, T. Wolf, H. V. Löhneysen, R. Sarkar, P. K. Biswas, H.-J. Grafe, and H. Kühne, Superconductivity of highly spin-polarized electrons in FeSe probed by ⁷⁷Se NMR, Phys. Rev. B **104**, 014504 (2021).

[59] W. Li, Y. Zhang, P. Deng, Z. Xu, S.-K. Mo, H. Yi, H. Ding, M. Hashimoto, R. G. Moore, D.-H. Lu, X. Chen, Z.-X. Shen, and Q.-K. Xue, Stripes developed at the strong limit of nematicity in FeSe film, Nat. Phys. **13**, 957 (2017).

[60] T. Watashige, Y. Tsutsumi, T. Hanaguri, Y. Kohsaka, S. Kasahara, A. Furusaki, M. Sigrist, C. Meingast, T. Wolf, H. V. Löhneysen, T. Shibauchi, and Y. Matsuda, Evidence for time-reversal symmetry breaking of the superconducting state near twin-boundary interfaces in FeSe revealed by scanning tunneling spectroscopy, Phys. Rev. X **5**, 031022 (2015).

[61] C.-L. Song, Y.-L. Wang, P. Cheng, Y.-P. Jiang, W. Li, T. Zhang, Z. Li, K. He, L. Wang, J.-F. Jia, H.-H. Hung, C. Wu, X. Ma,

X. Chen, and Q.-K. Xue, Direct observation of nodes and twofold symmetry in FeSe superconductor, Science **332**, 1410 (2011).

[62] C.-L. Song, Y.-L. Wang, Y.-P. Jiang, Z. Li, L. Wang, K. He, X. Chen, X.-C. Ma, and Q.-K. Xue, Molecular-beam epitaxy and robust superconductivity of stoichiometric FeSe crystalline films on bilayer graphene, Phys. Rev. B **84**, 020503(R) (2011).

[63] P. S. Wang, P. Zhou, S. S. Sun, Y. Cui, T. R. Li, H. C. Lei, Z. Q. Wang, and W. Q. Yu, Robust short-range-ordered nematicity in FeSe evidenced by high-pressure NMR, Phys. Rev. B **96**, 094528 (2017).

[64] Y. Zhang, M. Yi, Z.-K. Liu, W. Li, J. J. Lee, R. G. Moore, M. Hashimoto, M. Nakajima, H. Eisaki, S.-K. Mo, Z. Hussain, T. P. Devereaux, Z.-X. Shen, and D. H. Lu, Distinctive orbital anisotropy observed in the nematic state of a FeSe thin film, Phys. Rev. B **94**, 115153 (2016).

[65] L. Fanfarillo, J. Mansart, P. Toulemonde, H. Cercellier, P. Le Fèvre, F. Bertran, B. Valenzuela, L. Benfatto, and V. Brouet, Orbital-dependent Fermi surface shrinking as a fingerprint of nematicity in FeSe, Phys. Rev. B **94**, 155138 (2016).

[66] S. V. Borisenko, D. V. Evtushinsky, Z.-H. Liu, I. Morozov, R. Kappenberger, S. Wurmehl, B. Büchner, A. N. Yaresko, T. K. Kim, M. Hoesch, T. Wolf, and N. D. Zhigadlo, Direct observation of spin-orbit coupling in iron-based superconductors, Nat. Phys. **12**, 311 (2016).

[67] S. S. Huh, J. J. Seo, B. S. Kim, S. H. Cho, J. K. Jung, S. Kim, C. I. Kwon, J. S. Kim, Y. Y. Koh, W. S. Kyung, J. D. Denlinger, Y. H. Kim, B. N. Chae, N. D. Kim, Y. K. Kim, and C. Kim, Absence of Y-pocket in 1-Fe Brillouin zone and reversed orbital occupation imbalance in FeSe, Commun. Phys. **3**, 52 (2020).

[68] Y. Suzuki, T. Shimojima, T. Sonobe, A. Nakamura, M. Sakano, H. Tsuji, J. Omachi, K. Yoshioka, M. Kuwata-Gonokami, T. Watashige, R. Kobayashi, S. Kasahara, T. Shibauchi, Y. Matsuda, Y. Yamakawa, H. Kontani, and K. Ishizaka, Momentum-dependent sign inversion of orbital order in superconducting FeSe, Phys. Rev. B **92**, 205117 (2015).

[69] M. D. Watson, T. K. Kim, A. A. Haghighirad, S. F. Blake, N. R. Davies, M. Hoesch, T. Wolf, and A. I. Coldea, Suppression of orbital ordering by chemical pressure in FeSe$_{1-x}$S$_x$, Phys. Rev. B **92**, 121108(R) (2015).

[70] R. M. Fernandes and O. Vafek, Distinguishing spin-orbit coupling and nematic order in the electronic spectrum of iron-based superconductors, Phys. Rev. B **90**, 214514 (2014).

[71] A. I. Coldea, S. F. Blake, S. Kasahara, A. A. Haghighirad, M. D. Watson, W. Knafo, E. S. Choi, A. McCollam, P. Reiss, T. Yamashita, M. Bruma, S. C. Speller, Y. Matsuda, T. Wolf, T. Shibauchi, and A. J. Schofield, Evolution of the low-temperature Fermi surface of superconducting FeSe$_{1-x}$S$_x$ across a nematic phase transition, npj Quantum Mater. **4**, 2 (2019).

[72] P. Zhang, P. Richard, T. Qian, Y.-M. Xu, X. Dai, and H. Ding, A precise method for visualizing dispersive features in image plots, Rev. Sci. Instrum. **82**, 043712 (2011).

[73] Z. Li, J.-P. Peng, H.-M. Zhang, W.-H. Zhang, H. Ding, P. Deng, K. Chang, C.-L. Song, S.-H. Ji, L. Wang, K. He, X. Chen, Q.-K. Xue, and X.-C. Ma, Molecular beam epitaxy growth and post-growth annealing of FeSe films on SrTiO$_3$: A scanning tunneling microscopy study, J. Phys.: Condens. Matter **26**, 265002 (2014).

[74] W. H. Zhang, X. Liu, C. H. P. Wen, R. Peng, S. Y. Tan, B. P. Xie, T. Zhang, and D. L. Feng, Effects of surface electron doping and substrate on the superconductivity of epitaxial FeSe films, Nano Lett. **16**, 1969 (2016).

[75] R. Zhou, D. D. Scherer, H. Mayaffre, P. Toulemonde, M. W. Ma, Y. Li, B. M. Andersen, and M.-H. Julien, Singular magnetic anisotropy in the nematic phase of FeSe, npj Quantum Mater. **5**, 93 (2020).

[76] C. G. Wang, Z. Li, J. Yang, L. Y. Xing, G. Y. Dai, X. C. Wang, C. Q. Jin, R. Zhou, and G.-Q. Zheng, Electron mass enhancement near a nematic quantum critical point in NaFe$_{1-x}$Co$_x$As, Phys. Rev. Lett. **121**, 167004 (2018).

[77] K. Ueshima, F. Han, X. Zhu, H.-H. Wen, S. Kawasaki, and G.-Q. Zheng, Magnetism and superconductivity in Sr$_2$VFeAsO$_3$ revealed by ^{75}As- and ^{51}V-NMR under elevated pressures, Phys. Rev. B **89**, 184506 (2014).

[78] S. Kawasaki, T. Mabuchi, S. Maeda, T. Adachi, T. Mizukami, K. Kudo, M. Nohara, and G.-Q. Zheng, Doping-enhanced antiferromagnetism in Ca$_{1-x}$La$_x$FeAs$_2$, Phys. Rev. B **92**, 180508(R) (2015).